INSTITUTE OF PHYSICS PUBLISHING JOURNAL OF PHYSICS D: APPLIED PHYSICS

J. Phys. D: Appl. Phys. **37** (2004) 595–609 PII: S0022-3727(04)65734-2

Advances in low-voltage circuit breaker modelling

B Swierczynski, J J Gonzalez, P Teulet, P Freton and A Gleizes

CPAT, UMR CNRS 5002, Université Paul Sabatier, 118 route de Narbonne, 31062 Toulouse, Cedex, France

E-mail: gonzalez@cpat.ups-tlse.fr

Received 7 July 2003
Published 28 January 2004
Online at stacks.iop.org/JPhysD/37/595 (DOI: 10.1088/0022-3727/37/4/011)

Abstract
This paper is devoted to the study of electric arc behaviour under the influence of an external magnetic field. This situation is close to that occurring in a low-voltage circuit breaker where an arc, after ignition, is submitted to the magnetic field of the circuit. After a discussion of the literature, we present our contribution. Two different methods are compared to take the magnetic effects into account. Arc displacement in the geometry studied is dealt within a specific development presented in this paper. We show the influence of the nature of the gas on the arc velocity and on possible re-strike using air and an air–PA6 mixture as the plasma gas.

1. Introduction

Numerous papers study the influence of external forces on arc behaviour [1–3]. More particularly, in high-voltage circuit breakers, these forces are convective ones used to blow the arc during the passage to zero current [4]. In low-voltage circuit breakers, they can come from the contribution of the magnetic field created by the external electric circuit [5, 6]. In this paper, we focus our attention on this last application.

Investigations into arc behaviour in low-voltage circuit breakers are of great relevance to the switching industry: they give important information for designers to improve the performance of devices. Low-voltage circuit breakers are used to protect the power supply to electrical machines and to protect people as well as electrical equipment against a default current. In this kind of breaker, the voltage is about 1 kV and the current intensity in the range of some kiloamps. Its main function is to conduct and to switch off the electrical current. When a default current occurs, the contacts are separated by mechanical and/or magnetic forces. During the switching operation, an electrical arc is created between two contacts. In most cases the arc starts to burn after a short lag time due to the magnetic blow field of the current flowing towards the contact pieces [7]. Then the arc reaches a quenching area, consisting of steel splitter plates. During its life-time, several phases need to be considered. First, separation of the contacts, with their opening velocity, then arc movement in the chamber and finally re-strike or cutting in the splitter plates. During these three main phases, a lot of physical mechanisms act in the device like pressure, radiation, convection, conduction, melting/vapourization of contact material and magnetic forces.

In order to describe and to predict arc behaviour and the various characteristic quantities in the arc chamber of the circuit breaker, several approaches can be used: the experimental way [8, 9], black box simulation and also the magnetohydrodynamic (MHD) approach [7, 10]. Although a lot of information can be obtained by the two first approaches, optimization and dimensionless studies pose numerous problems. So, the MHD approach seems to be the most complete way to consider a lot of physical mechanisms occurring in low-voltage circuit breakers. Nevertheless, the global model of the arc and of the switching process in the low-voltage circuit breaker remains incomplete due to the complexity of its geometry, which requires a three-dimensional coordinate system, and to the inter-dependent physical phenomena involved. Generally, models do not take into account all the phenomena and use extensive approximations, first, to simplify the problem, and second, to decrease the calculation time. These approximations mainly concern interactions with the walls (erosion, ablation), description of the arc movements and the influence of the magnetic effects on the arc. For the calculation time, one heavy operation is calculating the magnetic field over the whole domain. In effect, the magnetic field self-induced by the arc and at the same time the circuit contribution have to be taken into account.

Various experimental and theoretical papers report the study of low-voltage circuit breakers: the theoretical ones are

numerous. A first paper of Daube *et al* [11] proposes an overview of the physical effects to be taken into account. In this paper, after a general description, a three-dimensional model is presented. One of the difficulties underlined by the authors is the calculation time. However, the arc zone is not well represented, and an arbitrary initial arc volume is given, allowing the use of a symmetry axis for the plasma zone. There is no arc movement and the external magnetic field is not taken into account. The magnetic field created by the arc is calculated by the Biot–Savart Law. With all the assumptions, the 100 μs of the simulated arc require a computing time of 14 days on a single processor workstation [11]. Other authors like Schlitz *et al* [2, 12] also present studies on the subject. In their first paper, the bases of the model are given in a simple free burning arc configuration. This configuration is used by the authors to validate the model in a stationary configuration. In their second paper, the configuration is closer to reality, but the arc root positions stay the same during time. In the same way, the external magnetic field is not calculated but imposed, and the authors show the influence of its value on the arc behaviour such as the increase in the voltage due to arc bending. In Lindmayer's [13] and Barcikowski's [14] papers, the external magnetic field is calculated by the Biot–Savart Law, and the arc attachment conditions depend on the rail/plasma interface by a heating flux balance. These authors always made the assumption of a symmetry plane for calculations in their geometry. For arc attachment, a current density distribution, a function of the temperature in the boundary element near the rail, is considered. This is done assuming that only the hottest neighbouring areas of the electrode contribute to the current emission. So, locally, depending on the temperature field, the current density distribution is divided over several hottest areas. Another numerical study by Essiptchouk [15] deals with arc movement and root velocity under the action of an external magnetic field. In this paper, the physics is on the balance between the Lorentz force and the aerodynamic drag force. It concerns a rotating arc and shows the change in velocity during time due to the energy transfer to the anode. So, this theory is difficult to apply in a low-voltage circuit breaker device.

Concerning experimental papers, few exist in the literature. Keldar's study [1] is related to the arc bending on a transversal flow. Some experimental papers on arc root velocity determination in low-voltage circuit breaker devices also exist [16, 17]. In these papers, the determination of the velocity is based on an analysis of the magnetic induction created by the arc motion from the outside of a breaking system at numerous points. By this method, the authors determine the position of the average line of current that magnetically represents the arc.

In this paper, we report our contribution to represent the arc behaviour in a low-voltage circuit breaker. A three-dimensional computational model of the arc is described in a simplified geometry. A commercial computational fluid dynamics code (Fluent 4.5) has been adapted and modified to model a fully coupled air plasma flow and the total magnetic field due to the arc and to the contribution of the electrodes. Due to the physical complexity and to the geometry of the low-voltage circuit breaker, several hypotheses have been used in this paper, and the opening and cutting phases are not considered. We focus our attention on the arc behaviour between the contacts.

First, we present briefly in section 2 the calculation of the composition and transport properties for different mixtures of air with the composite material vapours used in this study. Second, the stationary model and results in several air–%PA6 media are presented (section 3).

Specific developments for the external magnetic field and for the moving arc phenomena necessary to describe the transient state are proposed.

Finally, the results for the transient state, including the above developments, are discussed in section 4.

2. Transport properties

2.1. Introduction

In a low-voltage circuit breaker, before the appearance of default currents, only air is present in the chamber. When an electric problem occurs, the presence of the arc leads to various species in the breaker: during and after arc ignition, metal vapour coming from the erosion of the rails diffuses in the chamber. After circuit opening, the arc moves to the splitters under pressure and magnetic forces. So, the interactions with the walls produce a mixture of air with PA6 vapour, the basic monomer of PA6 being $C_6H_{11}O_1N_1$. These organic vapours play an important role because they can affect the gas flow and re-strikes of the arc. The literature reports methods for determining vapour production in low-voltage [18] and high-voltage circuit breakers [19, 20].

In this paper, we do not plan to describe all the ablation and erosion mechanisms, but in order to study the influence of vapour on arc behaviour, several homogeneous gas mixtures will be considered.

2.2. Method

The first step to obtain the transport coefficients is the calculation of the equilibrium composition and thermodynamic properties of the plasma. Some papers dealing with the determination of these parameters in plasmas formed of material ablated from circuit breaker walls have already been published [21, 22].

For this paper, the methods based upon the mass action law and the chemical base concept described by Godin and Trépanier [23, 24] were used to determine the plasma compositions. Three cases were investigated: pure air and 95% air–5%PA6 and 90% air–10%PA6 mixtures. We did not take into account the formation at low temperature of condensed species such as graphite.

Figure 1 presents the results obtained for a 90% air–10%PA6 plasma for temperatures under 30 000 K. Between 300 and 5000 K, we can see the presence of various carbon-containing gases such as CO, CO_2, C_2H_2, CHN and CH_4. For temperatures higher than 5000 K, all the dissociations have been completed and only pure components like O, C, N and H and their ions are present in the plasma.

Knowledge of the equilibrium composition allows the thermodynamic properties to be calculated: mass density, ρ (Kg m^{-3}), enthalpy, H (J Kg^{-1}), and specific heat at constant pressure, C_p (J Kg^{-1} K^{-1}). The mass density and the enthalpy

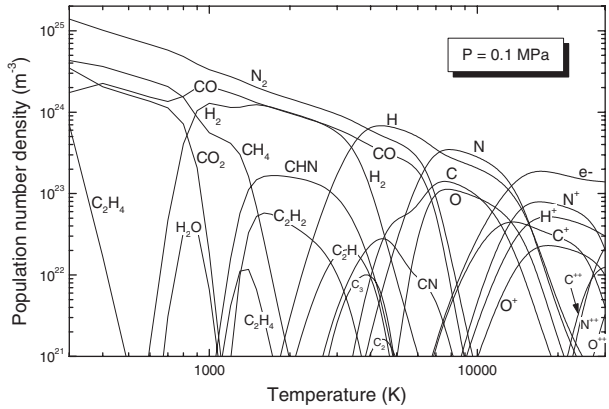

Figure 1. Equilibrium composition of a 90% air–10%PA6 plasma.

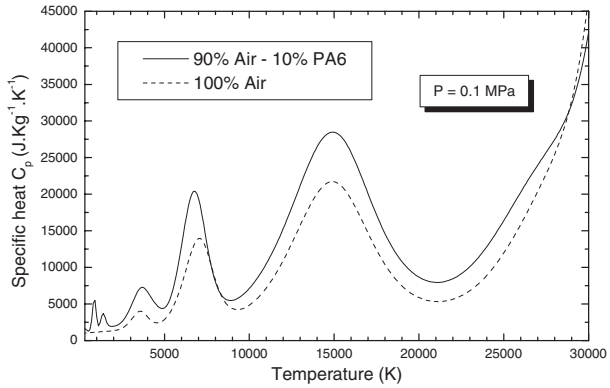

Figure 2. Comparison of the specific heats of pure air and 90% air–10%PA6 plasmas.

are directly obtained from the equilibrium composition, and the specific heat, C_p, is calculated as a numerical derivative of the enthalpy [25]. As an example, the specific heats of air and 90% air–10%PA6 plasmas are compared in figure 2. In the case of air, the four peaks located at 3500 K, 7000 K, 15 000 K and 30 000 K are due, respectively, to the dissociation of O_2, the dissociation of N_2 and the first and second ionization of N and O atoms. For the 90% air–10%PA6 plasma, the two first peaks situated at 900 and 1300 K come from the dissociation of CO_2 and CH_4 polyatomic molecules (figure 1). The two following at 3700 K and 6800 K are due, respectively, to the dissociation of H_2 and the dissociation of N_2 and CO. The last two at 15 000 and 30 000 K are the consequence of the first and second ionization of carbon and nitrogen atoms.

Knowing the equilibrium composition and the thermodynamic properties, the transport coefficients (viscosity, η (Kg m^{-1} s^{-1}), and electrical, σ (S m^{-1}), and thermal, K (W m^{-1} K^{-1}), conductivities) are obtained by resolution of Boltzmann's integro-differential equation using the Chapman–Enskog method described in detail by Hirschfelder *et al* [26]. The expression used for calculation of viscosity has been reported in [26, 25]. The electrical conductivity is obtained from the work of Devoto [27, 28]. According to Vanderslice *et al* [29] and Devoto [27, 28], the thermal conductivity can be written as a sum of four terms: $K_{\mathrm{tot}} = K_{\mathrm{t}}^{\mathrm{h}} + K_{\mathrm{t}}^{\mathrm{e}} + K_{\mathrm{int}} + K_{\mathrm{reac}}$. The expressions for the translation thermal conductivities due to heavy particles, $K_{\mathrm{t}}^{\mathrm{h}}$, and to electrons, $K_{\mathrm{t}}^{\mathrm{e}}$, have been reported by Muckenfuss and Curtiss [30] and Devoto [31]. The internal thermal conductivity, K_{int}, was calculated by extension of the theory of Eucken [29]. The reaction thermal conductivity, K_{reac}, was deduced from the work of Butler and Brokaw [32]. The method of calculation and the detailed expressions for the transport coefficients can be found in [25].

To calculate the transport coefficients with the Chapman–Enskog theory, it is necessary to access a complete set of reduced collision integrals, $\bar{\Omega}^{(l,s)}$ [25, 26]. Calculation of these collision integrals differs according to the interaction potential between the two interacting chemical species:

(i) Neutral–neutral interactions: The collision integrals have been calculated with the fitting coefficients tabulated by [33] for Lennard-Jones (LJ) 6–12 potentials. If the force constants (σ and $\varepsilon/k_{\mathrm{B}}$) of the LJ potential were not available for a chemical species, the simple hard-sphere method was used [26].

(ii) Electron–neutral interactions: For this kind of interaction, according to Hirschfelder *et al* [26] and Chervy *et al* [25], the collision integrals are calculated with the effective transport cross section, $Q^{(l)}$, obtained from published momentum transfer cross sections.

(iii) Ion–neutral interactions: Two types of reactions must be considered: purely elastic collisions and resonant charge transfer. The latter process occurs when the neutral and ionized particles are of the same chemical species. According to Chervy [25], collision integrals, $\bar{\Omega}^{(l,s)}$, have been calculated considering only elastic collisions if $l = 2$ and only charge exchange if $l = 1$. For elastic collisions, the polarizabilities of the neutral species are necessary to calculate $\bar{\Omega}^{(l,s)}$. In this case, the general expression of the collision integrals given by [25] was based upon the works of Tan [34] and Kihara *et al* [35]. For charge exchange processes, more precise details concerning the collision integrals calculation can be found in [25].

(iv) Interaction between charged particles: A coulomb potential screened by the presence of charged particles was adopted in this work. Two cases were considered: attractive and repulsive potential, depending on the charge (+ or −) of the interacting species. The $\bar{\Omega}^{(l,s)}$ values obtained are based upon the work of Mason *et al* [36].

When collision integrals deduced from more accurate interaction potentials were found in the literature, we included these data in our calculations. We used the data published by [37] for e–$O_x^{(+)}$, e–$N_x^{(+)}$, e–$N_xO_y^{(+)}$ and $N_xO_y^{(+)}$–$N_xO_y^{(+)}$ interactions, by [38, 39] for e–C and C–$C_x^{(+)}$, by [40, 41] for e–H_x and H_x–$H_y^{(+)}$ and by [42] for C_xH_y–C_zH_w.

2.3. Results

A comparison of the results obtained for pure air and 90% air–10%PA6 is given in figures 3, 4 and 5 for electrical conductivity, σ, thermal conductivity, K, and viscosity, η, respectively.

For electrical conductivity, the difference at low temperatures ($T < 7000$ K) between the two curves is due to the presence of the NO molecule with pure air. This molecule has a low ionization potential (9.3 eV) leading to an increase in the electronic density and consequently in σ. As shown in figure 1, the NO molecule does not exist in

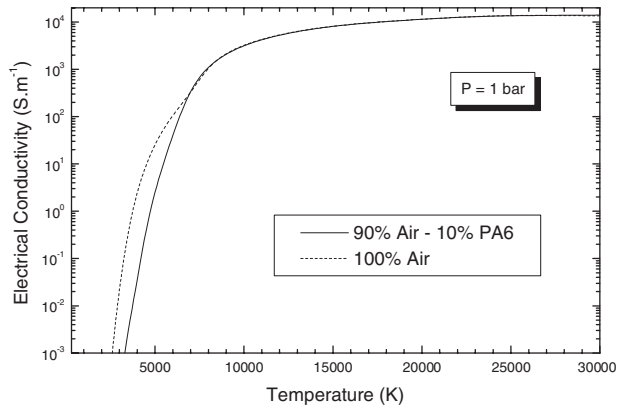

Figure 3. Comparison of electrical conductivity of air and 90% air–10%PA6.

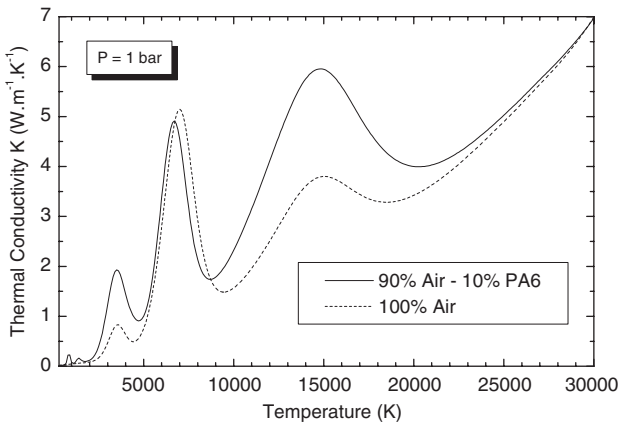

Figure 4. Comparison of thermal conductivity of air and 90% air–10%PA6.

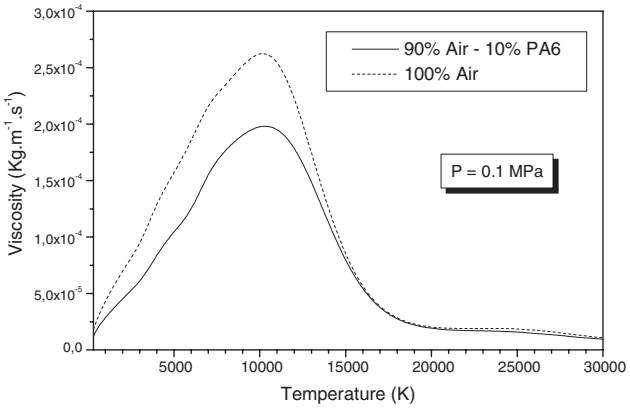

Figure 5. Comparison of viscosity of air and 90% air–10%PA6.

the 90% air–10%PA6 mixture because all the oxygen atoms are captured by carbon atoms to form carbon monoxide molecules, CO.

Figure 4 shows the results obtained for thermal conductivity. The existence of peaks from the reaction thermal conductivity, K_{reac}, can be explained exactly as for specific heat, C_p. The peak situated between 3000 and 4000 K is greater in the case of the air–PA6 mixture because of the high values of the collision integrals involving H_2. The peak around 7000 K takes similar values in the two cases because collision integrals for X–N_2 and for X–CO are of the same order of magnitude. The increase in the peak located at 15 000 K is due to elevated values of the collision integrals involving C and H species (e–C, e–H, e–C^+, e–H^+, C–C^+, H–H^+, ...). Likewise, the lower values of viscosities observed in figure 5 up to 14 000 K for air–PA6 plasma are due to the high values of the collision integrals for C and H species (e–C, e–H, ...).

These thermodynamic and transport coefficients will be used in the model to study the influence of the nature of the medium on the arc behaviour.

3. Stationary state

3.1. Numerical model

The developments of the model presented in this section have been validated previously [43, 44] for a free burning argon arc configuration. They have also been applied to several configurations, such as a cutting plasma torch [45], where a good agreement was found between theoretical and experimental results. So, we do not present here the validation step, which can be found in the published papers, but directly the hypothesis, the equations, the geometry and the results of the model applied to the low-voltage circuit breaker configuration.

The model is based on the finite volume method and uses the user defined subroutines of the commercial software Fluent version 4.5 to take the MHD effects into account.

3.1.1. Hypotheses. The model is based upon the following main assumptions:

(a) We ignore gravity.
(b) The medium is assumed to be plasma, which satisfies the conditions for local thermodynamic equilibrium.
(c) The plasma is a Newtonian fluid and the flow is laminar.
(d) The arc ignition is not modelled.
(e) The arc–electrode interaction is not taken into account.
(f) The three-dimensional model uses Cartesian geometry (x, y, z).

3.1.2. Equations. For the three-dimensional configuration, in the stationary state, the general equation used in the finite volume method can be written following the Patankar formulation [46]:

$$\frac{\partial}{\partial x}(\rho v_x \Phi) + \frac{\partial}{\partial y}(r v_y \Phi) + \frac{\partial}{\partial z}(r v_z \Phi) = \frac{\partial}{\partial x}\left(\Gamma_\Phi \frac{\partial \Phi}{\partial x}\right) + \frac{\partial}{\partial y}\left(\Gamma_\Phi \frac{\partial \Phi}{\partial y}\right) + \frac{\partial}{\partial z}\left(\Gamma_\Phi \frac{\partial \Phi}{\partial z}\right) + S_\Phi \quad (1)$$

x, y and z are the three directions of the coordinate system, and v_x, v_y and v_z are the respective velocities; ρ is the mass density. This general formulation can be used for all the equations by adjustment of the variable ϕ, of the diffusion coefficient, Γ_ϕ, and of the source term, S_ϕ. For example, the mass conservation equation can be obtained with $\phi = 1$, $\Gamma_\phi = 0$ and $S_\phi = 0$. In the same way, the values for the scalar potential equation used to determine the current densities are $\phi = V$ (potential), $\Gamma_\phi = \sigma$ (electrical conductivity) and $S_\phi = 0$ and no convection term. For the other equations, the different variables, ϕ,

Table 1. Equations in three-dimensions.

	ϕ	Γ_ϕ	S_ϕ
x momentum (2)	v_x	μ	$-\frac{\partial p}{\partial x}+\frac{\partial}{\partial y}\left(\mu\frac{\partial v_x}{\partial x}\right)+\frac{\partial}{\partial z}\left(\mu\frac{\partial v_z}{\partial x}\right)+\frac{1}{3}\frac{\partial}{\partial x}\left(\mu\frac{\partial v_x}{\partial x}\right)$ $-\frac{2}{3}\frac{\partial}{\partial x}\left(\mu\left(\frac{\partial v_y}{\partial y}+\frac{\partial v_z}{\partial z}\right)\right)+j_yB_z-j_zB_y$
y momentum (3)	v_y	μ	$-\frac{\partial p}{\partial y}+\frac{\partial}{\partial z}\left(\mu\frac{\partial v_y}{\partial y}\right)+\frac{\partial}{\partial x}\left(\mu\frac{\partial v_z}{\partial y}\right)+\frac{1}{3}\frac{\partial}{\partial y}\left(\mu\frac{\partial v_y}{\partial y}\right)$ $-\frac{2}{3}\frac{\partial}{\partial y}\left(\mu\left(\frac{\partial v_z}{\partial z}+\frac{\partial v_x}{\partial x}\right)\right)+j_zB_x-j_xB_z$
z momentum (4)	v_z	μ	$-\frac{\partial p}{\partial z}+\frac{\partial}{\partial x}\left(\mu\frac{\partial v_z}{\partial z}\right)+\frac{\partial}{\partial y}\left(\mu\frac{\partial v_y}{\partial z}\right)+\frac{1}{3}\frac{\partial}{\partial z}\left(\mu\frac{\partial v_z}{\partial z}\right)$ $-\frac{2}{3}\frac{\partial}{\partial z}\left(\mu\left(\frac{\partial v_x}{\partial x}+\frac{\partial v_y}{\partial y}\right)\right)+j_xB_y-j_yB_x$
Energy (5)	h	$\frac{\kappa}{C_p}$	$v_z\frac{\partial p}{\partial z}+v_x\frac{\partial p}{\partial x}+v_y\frac{\partial p}{\partial y}$ $+\mu\left[\begin{array}{l}2\left[\left(\frac{\partial v_x}{\partial x}\right)^2+\left(\frac{\partial v_y}{\partial y}\right)^2+\left(\frac{\partial v_z}{\partial z}\right)^2\right]\\+\left[\frac{\partial v_y}{\partial x}+\frac{\partial v_x}{\partial y}\right]^2+\left[\frac{\partial v_z}{\partial y}+\frac{\partial v_y}{\partial z}\right]^2+\left[\frac{\partial v_z}{\partial y}+\frac{\partial v_y}{\partial z}\right]^2\\-\frac{2}{3}\left[\frac{\partial v_x}{\partial x}+\frac{\partial v_y}{\partial y}+\frac{\partial v_z}{\partial z}\right]^2\end{array}\right]$ $+\frac{j_x^2+j_y^2+j_z^2}{\sigma}-4\pi\varepsilon_N+\frac{5}{2}\frac{k}{e}\left(\frac{j_x}{C_p}\frac{\partial h}{\partial x}+\frac{j_y}{C_p}\frac{\partial h}{\partial y}+\frac{j_z}{C_p}\frac{\partial h}{\partial z}\right)$
x potential vector (6)	A_x	1	$\mu_0.j_x$
y potential vector (7)	A_y	1	$\mu_0.j_y$
z potential vector (8)	A_z	1	$\mu_0.j_z$

Γ_ϕ and S_ϕ, used in the model are presented in table 1. In this table, P is the pressure, ε_N the net emission coefficient, μ the viscosity, κ the thermal conductivity and C_p is the specific heat.

Due to the presence of the arc in the medium, the self-induced magnetic field, $\vec{B}_s$, has to be calculated. By definition, $\vec{B}_s$ depends on the potential vector, $\vec{A}$, and

$$\vec{B}=\vec{\nabla}\wedge\vec{A} \tag{9}$$

We can thus obtain the magnetic field components, B_x, B_y and B_z, from the calculated potential vector components: A_x, A_y and A_z. The current density components are deduced from the scalar potential, V:

$$\vec{j}=-\sigma\vec{\nabla}V \tag{10}$$

In equations (2)–(10), the thermal and transport properties are functions of the local temperature and pressure. Radiation is taken into account by the net emission coefficient method. Simulation of the electric arc necessitates the inclusion of source terms in some equations: the Lorentz forces in the momentum equations (2)–(4) and the Joule effect and the radiation term in the energy equation (5).

3.1.3. Geometry and boundary conditions. As numerous physical mechanisms have to be considered, a simplified geometry (presented in figure 6) is used. This simplification of our geometry makes problem resolution easier, and similar simplified geometries can be found in various studies in [11, 7]. This geometry corresponds to a simplified experimental scale

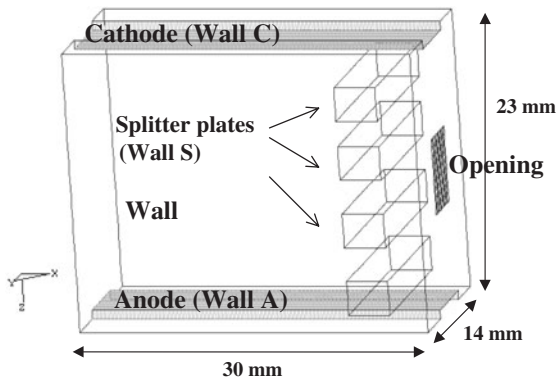

Figure 6. Low-voltage circuit breaker: simplified geometry.

model with performances not identical to the real ones but which allows us to analyse the main phenomena. Moreover, on a similar geometry, experimental tests have been made, allowing a partial validation. It includes a chamber, two rails and splitter plates. It consists of a parallelepipedic volume with one open area of about 25 mm^2 where static pressure equal to zero is imposed. We can also distinguish two rails 5.6 mm wide: wall C (for cathode) and wall A (for the anode).

The computational box is very small: 30 mm long, 23 mm high, and 14 mm wide. The dimensions used are similar to those used in the literature for the same study [17]. In this experimental paper the chamber is 42 mm long, 27 mm high and 10 mm wide.

On the right side, four blocks representing the splitters are included (wall S). The grid spacing is constant and equal to

Table 2. Boundary conditions for the three-dimensional transferred arc model.

Area	P	v_x	v_y	v_z	T	A_x	A_y	A_z	V
Opening	Static pressure	$\frac{\partial v_x}{\partial \vec{n}} = 0$	$\frac{\partial v_y}{\partial \vec{n}} = 0$	$\frac{\partial v_z}{\partial \vec{n}} = 0$	300	$\frac{\partial A_x}{\partial \vec{n}} = 0$	$\frac{\partial A_y}{\partial \vec{n}} = 0$	$\frac{\partial A_z}{\partial \vec{n}} = 0$	$\frac{\partial V}{\partial \vec{n}} = 0$
WALL	—	0	0	0	300	$\frac{\partial A_x}{\partial \vec{n}} = 0$	$\frac{\partial A_y}{\partial \vec{n}} = 0$	$\frac{\partial A_z}{\partial \vec{n}} = 0$	$\frac{\partial V}{\partial \vec{n}} = 0$
WALLA	—	0	0	0	3500	$\frac{\partial A_x}{\partial \vec{n}} = 0$	$\frac{\partial A_y}{\partial \vec{n}} = 0$	$\frac{\partial A_z}{\partial \vec{n}} = 0$	0 and $J(x, y)$
WALLC	—	0	0	0	3500	$\frac{\partial A_x}{\partial \vec{n}} = 0$	$\frac{\partial A_y}{\partial \vec{n}} = 0$	$\frac{\partial A_z}{\partial \vec{n}} = 0$	$\frac{\partial V}{\partial \vec{n}} = 0$ and $J(x, y)$
WALLS	—	0	0	0	1000 or $\frac{\partial T}{\partial \vec{n}} = 0$	$\frac{\partial A_x}{\partial \vec{n}} = 0$	$\frac{\partial A_y}{\partial \vec{n}} = 0$	$\frac{\partial A_z}{\partial \vec{n}} = 0$	$\frac{\partial V}{\partial \vec{n}} = 0$

0.16, 0.33 and 0.65, respectively, in the x, y and z directions. The calculation domain is made of about 2 65 000 computational cells. All the walls of the calculation domain have a temperature equal to 300 K, except the electrodes, where a mean temperature of 3500 K is assumed. An exponential profile of the current density is actually used as boundary conditions on walls C and A for the arc root attachment positions.

$$j_z(x, y) = J_{\max} \exp(-b\sqrt{x^2 + y^2}) \tag{11}$$

$J_{\max}$ is equal to 1.2×10^8 A m^{-2}, and b is a constant depending on the intensity. At the arc root attachments, we have $x = y = 0$. All the boundary conditions are summarized in table 2.

3.2. Results in stationary state

The results presented here concern different media for a current intensity equal to 100 A.

3.2.1. General results in air. The first series of results, presented in figures 7–9, is devoted to an arc in pure air for a current intensity of 100 A. All the results are presented in the central plane of the geometry. In this section, the contribution of the magnetic field induced by the rails is not taken in account. Figure 7 represents the temperature field obtained. In this case, the arc root positions (upper and lower) are imposed in the middle of the rails. Due to the geometry and to the small area of the exhaust, hot temperatures over 4000 K can be found throughout the geometry, with a maximum temperature around 20 kK in the arc core region. The stationary results presented will be used as the initial condition for the transient state. Some authors use an arbitrary gas volume with a hot temperature as initial values [7, 11]. With this last consideration, the arc chamber is not pre-heated by radiation, convection or conduction as in our case, but the disadvantage is that the energy quantity introduced cannot be governed.

The potential field is presented in figure 8. It represents the drop voltage in the column and does not take into account the anode fall voltage or the electron work function. A reference potential of zero is imposed on the anode, and we found a maximum value of 25 V near the cathode.

Finally, in this first series of results in an air medium, figure 9 reports the velocity field magnitude in the geometry. As the geometry is practically closed, convection is only due to the Lorentz forces created by the magnetic field self-induced by the arc. A maximum value around 140 m s^{-1} is found near the contacts due to the area of the arc attachments. Near the cathode, these forces pump the gas down, while near the anode, the same forces pump the gas to the top. This explains the existence of a stagnation point at the centre of the geometry.

3.2.2. Influence of medium on arc characteristics. As explained in section 2, in real circuit breakers, before arc ignition the chamber contains only air at atmospheric pressure. When the arc is created and during the displacement phase, metallic and organic vapours appear, coming from the erosion of the contacts and from the plastic walls, respectively. At this step of the study, we do not use a specific model to take this erosion into account; nevertheless, in order to study the influence of the medium on the arc behaviour, we tested three homogeneous mixtures: air, air–5%PA6 and air–10%PA6. The current intensity is equal to 100 A. For the three media, we present in figures 10(*a*) and (*b*) the temperature evolution along the rail direction, respectively, close to the upper rail ($Z = 2.63$ mm) and close to the downstream one ($Z = 18.4$ mm). The curves are plotted from the left to the maximum temperature position of the arc. With an air–PA6 plasma, we can note two changes in the profiles corresponding to the dissociation of nitrogen and oxygen. The column drop voltage increases with the PA6 proportion. The total column voltage is equal to 25.02, 28.15 and 35.02, respectively, for air, air–5%PA6 and air–10%PA6 media. So, for the same intensity, the power injected into the plasma is not the same. Nevertheless, small differences can be observed between the curves, except between 3000 and 7000 K. The curves are close for the arc core, and differences appear at the edges with lower temperatures in an air–10%PA6 mixture. The presence of organic vapours in the plasma seems to cool the edges of the arc. The results for the three mixtures in the stationary state will be used in the transient state as initial conditions for the time $t = 0$.

3.2.3. Arc under external magnetic field. The literature reports studies showing the influence of an external magnetic

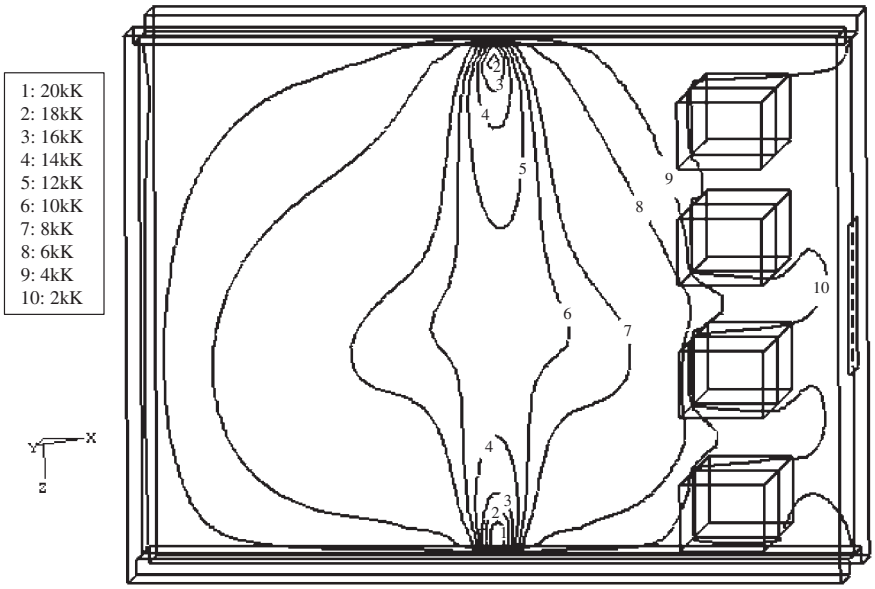

Figure 7. Temperature field (K) in air plasma; $I = 100$ A; stationary state.

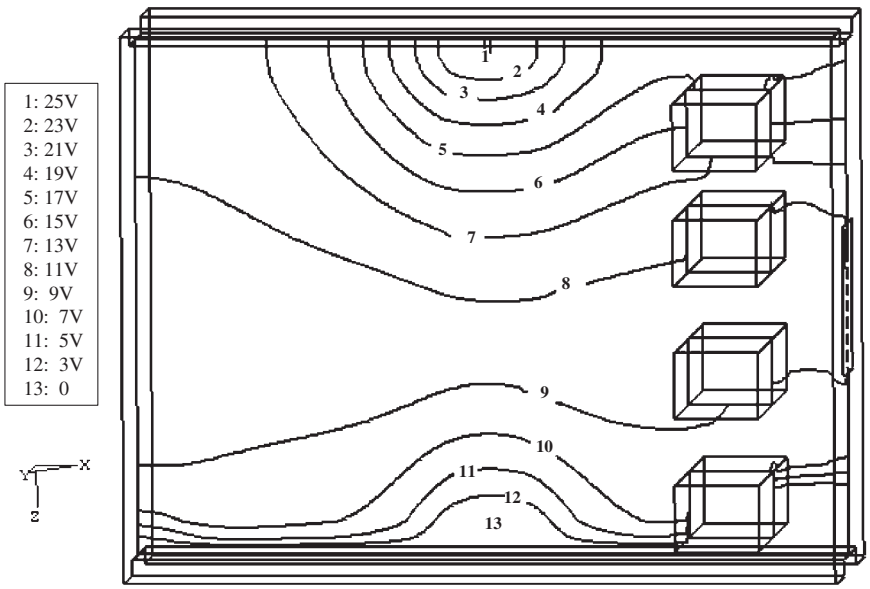

Figure 8. Scalar potential field (V) in stationary state; air plasma; $I = 100$ A.

field on arc bending [2, 3]. As, in the low-voltage circuit breaker, the arc is submitted to the magnetic field coming from the current in the contacts, we applied a constant value of the magnetic field, B_c, to the arc plasma in order to study its influence. Table 3 presents the results for a current intensity of 100 A, and B_c is equal to 2 and 5 mT. For the three plasma media, air, air–5%PA6 and air–10%PA6, and the two values of the external applied magnetic field, we give the column drop voltage and the δx quantities. The δx values correspond to the arc displacement in the plane $y = 0$ under the influence of the magnetic field from the natural position and are determined in the middle distance between the two electrodes through the position of the maximum axial current density. Two comments can be made: first, the voltage drop increases with the value of the external magnetic field and with the proportion of the PA6 component in the air. Indeed, when a greater value of the magnetic field is applied, the arc becomes lengthened and so an increase in the drop voltage occurs. Second, a greater increase in the drop voltage is observed for the same arc bending with the proportion of PA6: the electrical conductivity increases at low temperatures, leading to an augmentation of the energy losses, which for a given current intensity value increases the electrical field and so the drop voltage.

4. Transient state

4.1. Numerical model

In order to study the displacement of the arc in the chamber, we need to extend our model to transient states.

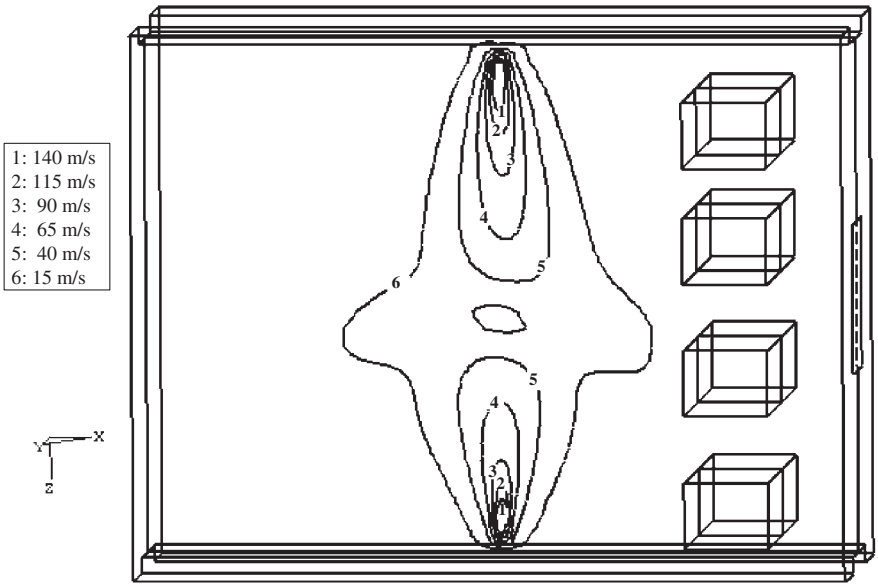

Figure 9. Velocity field magnitude (m s^{-1}) in stationary state; pure air; $I = 100$ A.

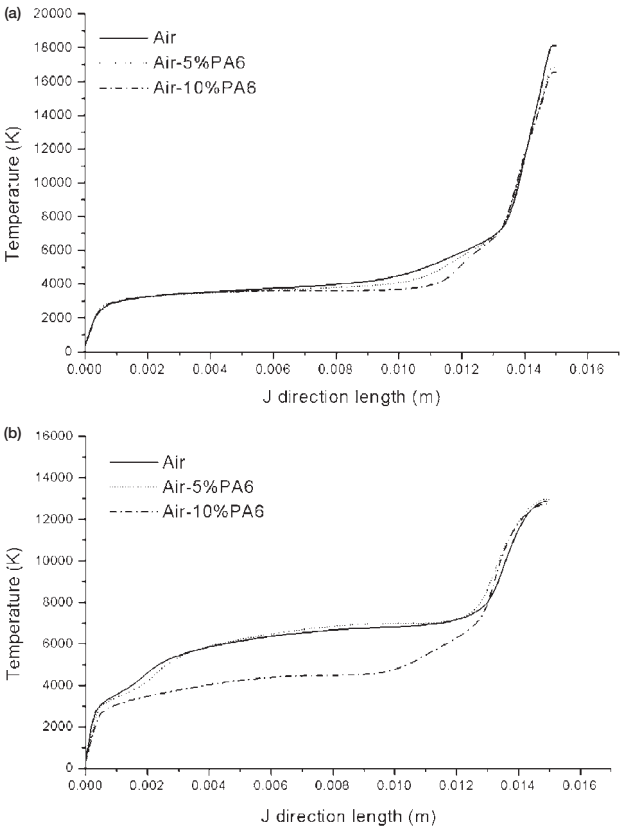

Figure 10. (*a*) Temperature evolution along the rail direction on the section $Z = 2.63$ mm. (*b*) Temperature evolution along the rail direction on the section $Z = 18.4$ mm.

The main assumptions are those presented in the stationary case, and the other hypotheses for the transient state are:

(a) at $t = 0$, we switch on the magnetic field due to the contact.
(b) the arc roots position can move independently.
(c) erosion is neglected.

Table 3. Influence of the external magnetic field value on the voltage drop and arc bending for three media; $I = 100$ A.

	Air	Air–5%PA6	Air–10%PA6
$B_c = 0$	$\mathrm{d}\mathrm{d}p = 25.02$	$\mathrm{d}\mathrm{d}p = 28.15$	$\mathrm{d}\mathrm{d}p = 35.02$
	$\delta x = 0$	$\delta x = 0$	$\delta x = 0$
$B_c = 2$ mT	$\mathrm{d}\mathrm{d}p = 25.25$	$\mathrm{d}\mathrm{d}p = 41.6$	$\mathrm{d}\mathrm{d}p = 60.93$
	$\delta x = 4.48$	$\delta x = 4.64$	$\delta x = 6.14$
$B_c = 5$ mT	$\mathrm{d}\mathrm{d}p = 29.67$	$\mathrm{d}\mathrm{d}p = 60.8$	$\mathrm{d}\mathrm{d}p = 108.75$
	$\delta x = 6.47$	$\delta x = 6.97$	$\delta x = 7.47$

The time $t = 0$ corresponds to the results found by the stationary study. When the transient model begins, the external magnetic field contribution given by the contacts is switched on. In reality, the external magnetic field acts during arc ignition, and we can assume that the arc is bent and that it jumps during contact opening.

4.1.1. Modifications of the equations. The temporal term is added in the general equation:

$$\frac{\partial \rho\phi}{\partial t} + \mathrm{div}(\rho\vec{v}\phi) = \mathrm{div}(\Gamma_\phi \overrightarrow{\mathrm{grad}}(\phi)) + S_\phi \qquad (12)$$

The formulation of the current density is changed and is given by

$$\vec{j} = \sigma\vec{E} - \frac{\partial \vec{A}}{\partial t} \qquad (13)$$

During the displacement of the arc, we need to calculate the contribution of the magnetic field due to the contact. This is one of the crucial points underlined by other authors [5–10]. Another crucial point is the description of the arc displacement in the chamber under the combined effect of convective, pressure and magnetic forces. So in the next section we present the specific methods that we developed to deal with these two problems.

4.2. Specific developments

4.2.1. Approach for magnetic field calculation

Introduction. The self-induced magnetic field, $\vec{B}_s$, created by the arc is an important phenomenon. Near the cathode, it governs the pumping of the surrounding gas in the plasma core. More generally, the magnetic field leads to the pressure forces that we need to incorporate in the momentum equations. In the low-voltage circuit breaker device, the arc is under the influence of $\vec{B}_s$ but also the magnetic field, $\vec{B}_c$, from the contribution of the contacts due to current circulation. The total magnetic field, $\vec{B}$, in the chamber is thus the sum of $\vec{B}_s$ and $\vec{B}_c$.

The current carrying path between the contact and the arc generates a loop effect that moves the arc to the quenching chamber. If we want to represent this effect, current conservation must be assumed between the material contacts and the plasma. Generally, the transition between the two media is not modelled, and a current density distribution or a constant value is assumed in the rails.

One way of obtaining the total magnetic field at all the points of the calculation domain is to use the Biot–Savart Law:

$$\vec{B} = \frac{\mu_0}{4\pi} \iiint_{\text{domain}} \vec{j}(\vec{r}') \times \frac{\vec{r} - \vec{r}'}{|\vec{r} - \vec{r}'|^3} \, \mathrm{d}^3 r' \qquad (14)$$

The advantage of the Biot–Savart Law is that it can be applied to various complex geometries, but on the other hand the calculation time is long [11].

This method can be used to calculate the magnetic field contribution of the rails and the self-induced magnetic field due to the plasma. Nevertheless, we can see (equation (14)) that the magnetic field at one point results from the contribution of all the other points of the calculation domain. Consequently, obtaining results is considerably slowed down. For example, for our 260 000 cells, this requires $260\,000^2$ operations. So, in order to gain calculation time, we propose to obtain the total magnetic field without using the Biot–Savart formulation.

Proposed approach. One way to shorten the calculation time consists of considering the contributions of the plasma and the contacts to the total magnetic field (respectively, $\vec{B}_s$ and $\vec{B}_c$) separately. In the plasma the potential vector is calculated to obtain $\vec{B}_s$; three new scalar equations (equations (6)–(8)), one for each vector component, are introduced and solved for each iteration.

The potential vector method in the plasma could be combined with the Biot–Savart formulation in the electrodes. The number of points, r', to consider would be then lower than in the case of the use of the Biot–Savart formulation in all the domain. The points, r', should be restricted to the points of the rails covered by the current density. Nevertheless, the number of operations, depending on the grid spacing and on the length of the rails covered by the current intensity, will be higher than in the proposed approach.

This vector potential method will be used only in the plasma domain, and we will use another method for the rail contributions, $\vec{B}_c$.

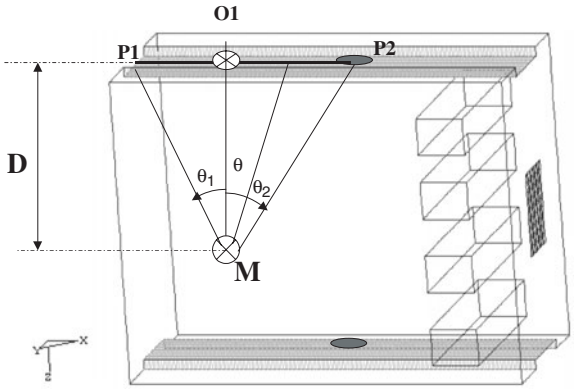

Figure 11. Schema of the magnetic field contribution due to the electrode (upper rail contribution).

The electrodes can be assumed to be rectilinear segments with a given length, and it is then possible to use equation (15).

$$\vec{B}_1(M) = -\vec{e}_{y'} \frac{\mu_0 I}{4\pi D} (\sin(\theta_2) - \sin(\theta_1)) \qquad (15)$$

Practically, the total calculation geometry is divided in domains: 'live cells' for the plasma region and 'wall cells' for the conducting material. Calculations loops are made on the geometry, and following the domain, the potential vector method or equation (15) is used, and the total magnetic field at each point corresponds to both contributions.

The magnetic field contribution of the rail to one point can be deduced directly with only three parameters: two angles and one distance.

For each new position of the arc roots at the cathode and anode, the contributions of the two contacts are determined. For all the points of the plasma domain, we calculate the contribution of the two rails as presented for the upper one in figure 11. Over time, the contribution of the rail is re-calculated only if the arc root positions change, that is to say if the segment length of the current intensity is modified (distance between P1 and P2 in figure 11).

We compared the results obtained by the Biot–Savart and the rectilinear segment formulations. In this calculation, the current intensity is equal to 100 A, and only the upper rail contribution is presented. The results are presented in figures 12 and 13 for the Biot–Savart formulation and for the rectilinear segment formulation, respectively. For all the tests, the wide segment corresponds to one cell in the y-direction and is associated to 100 A, that is to say that when we compared the two approaches for 800 A, we took eight cells in the y-direction. We can see (figures 12 and 13) that the two kinds of result are very similar, except close to the segment. So, due to the time difference (more than five-fold) between the two approaches and the small differences in the results, we chose to use the segment formulation presented in figure 11 in our developments.

4.2.2. Method for the moving arc model

Introduction. In the arc chamber due to convective, pressure and magnetic forces, the arc moves between the two contacts.

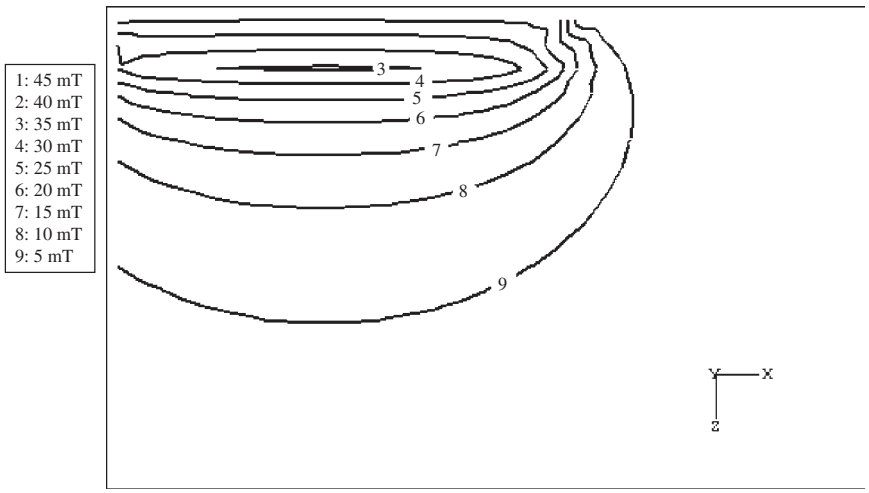

Figure 12. Magnetic field (T) obtained by the Biot–Savart Law.

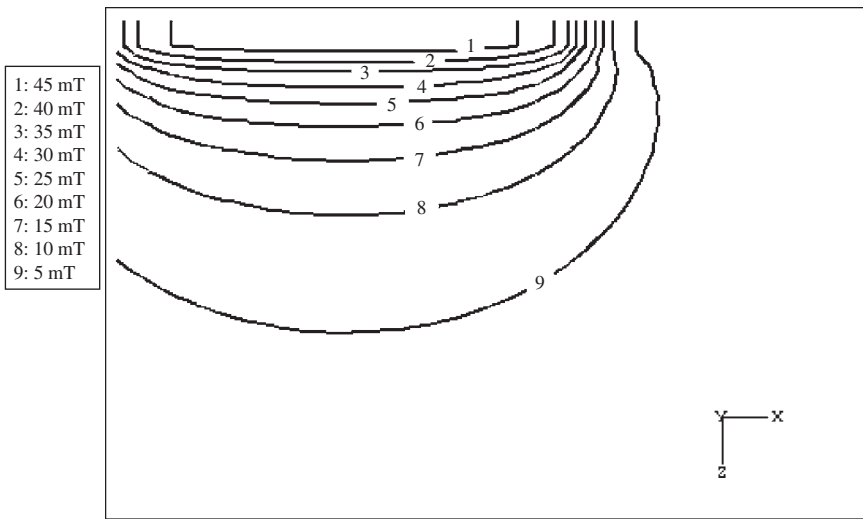

Figure 13. Magnetic field (T) obtained by the rectilinear segment formulation.

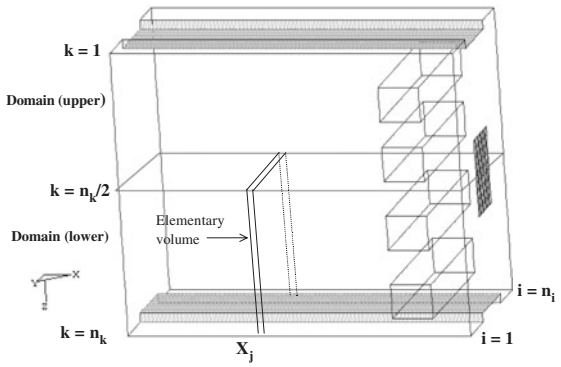

Figure 14. Description of separation of the geometry in various slices to enable a self-coherent displacement of the arc.

The literature only reports few complete studies where the arc root can move [5–13]. Nevertheless, on the proposed approaches, the arc motion is not correlated with the characteristics of the medium.

The aim of our study concerning this point is not to represent all the physical mechanisms occurring in the arc motion but to propose a model able to represent an arc movement taking into account parameters as the local gas temperature or the local electrical conductivity. The physical model proposed here is based on the literature on high-voltage circuit breakers [47, 48] and plasma torches [49]. In the first case, around current zero, the models predict from an applied transient recovery voltage the interruption capability of the system (the existence of the arc). The theory is based on the global conductance corresponding to the integrated value of the electrical conductivity in the chamber directly correlated to the mean electrical conductivity. In plasma torch models, the arc attachment is located in the cylindrical hollow anode at a position depending on the values of the current intensity and the gas mass flow rate. The mean arc attachment position is then determined by the Steenbeck minimum principle [50]. But this theory is only used in the two-dimensional model because in the three-dimensional model the arc length does not allow us to know its position along the angular direction. In order to determine the three-dimensional arc position, the theory is based on the gradient potential and on the mean electrical conductivity. Using this theory, the

arc fluctuations and the movement frequency were compared with experimental measurements, and a good agreement was found [49]. The proposed approach is based on these two examples.

Proposed approach. As arc root movement does not vary linearly inside the real device and cannot be described by simple analytic laws, it seems important to be able to propose a model of self-acting displacement of the arc in the geometry. So, we use a method that enables determination of the most probable positions of arc attachment at the anode and the cathode. This is done by horizontally dividing the chamber into two calculation domains (upper and lower) as presented in figure 14. For each domain, at each time step, the mean conductivity (equation (16)) is calculated on elementary slices along the direction of arc movement (Ox) to define the most probable position for attachment: integration is only made on the plasma cells.

$$\bar{\sigma}_{\text{upper}}(X) = \int_1^{nk/2}\int_1^{ni} \sigma \frac{\mathrm{d}V}{N} \qquad \bar{\sigma}_{\text{lower}}(X) = \int_{nk/2}^{nk}\int_1^{ni} \sigma \frac{\mathrm{d}V}{N} \tag{16}$$

where N is the number of plasma cells in the given slice.

At each time step during calculation, the elementary volume presenting the highest mean conductivity is chosen for the next position of arc attachment. For a given attachment, due to the arc bending under the influence of the magnetic forces, the new position is close to the attachment position. Nevertheless, the presented method allows the arc to re-strike at any other position if the conditions are satisfied. The anodic and cathodic positions are independently determined, and the current density distribution given by equation (11) is applied

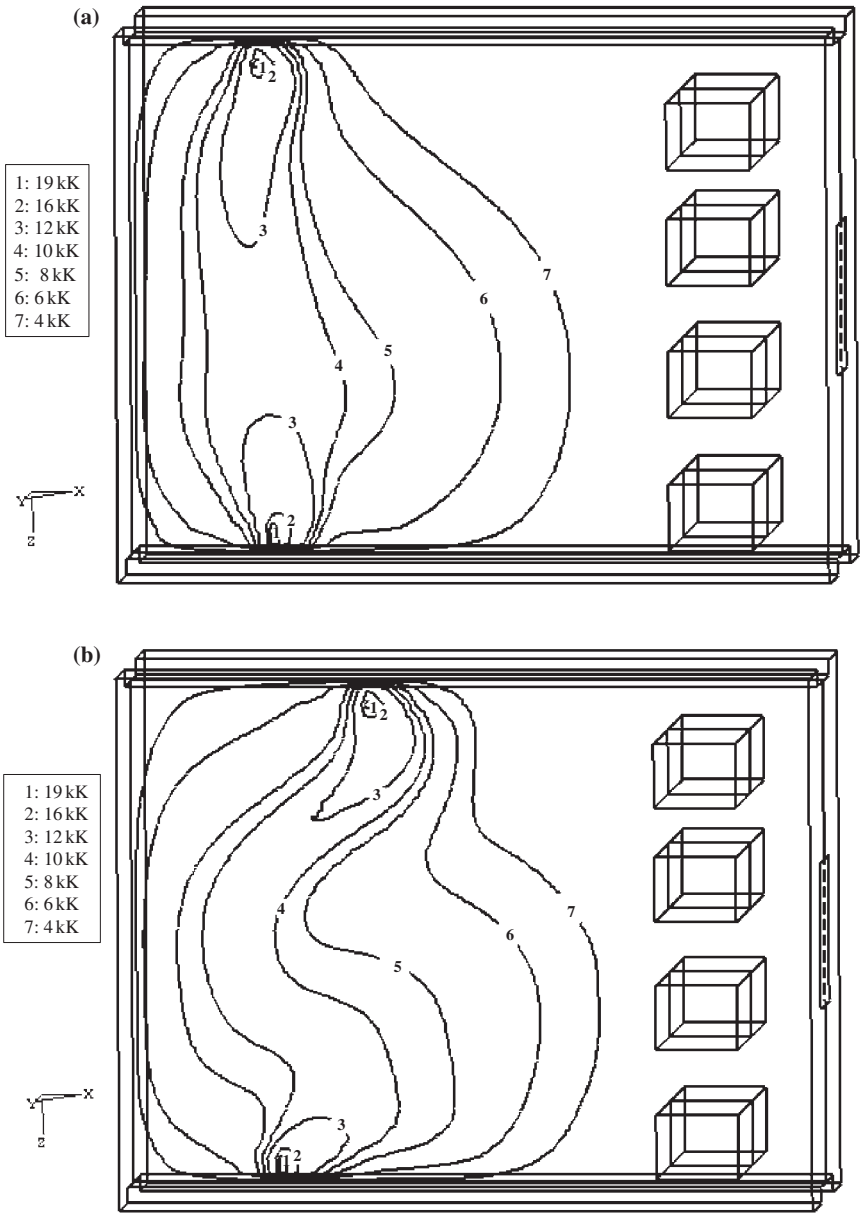

Figure 15. Temperature fields in air; (*a*) $t = 40\,\mu$s, (*b*) $t = 310\,\mu$s ($I = 100$ A; autonomous arc root velocity).

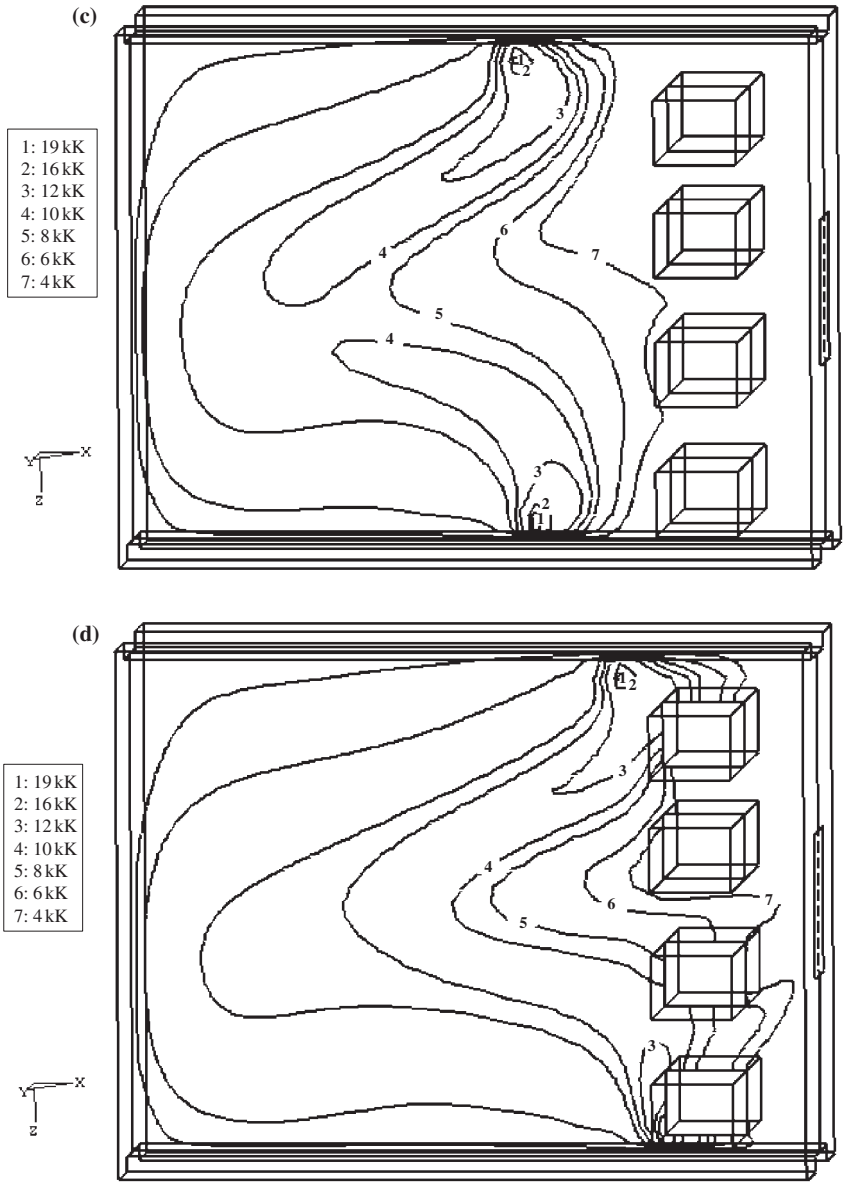

Figure 15. Temperature fields in air; (*c*) $t = 580\,\mu$s, (*d*) $t = 870\,\mu$s ($I = 100$ A; autonomous arc root velocity).

on both electrodes centred on the determined position. The current intensity in the electrodes then flows from the edge of the calculation domain, P1, to the new position of the arc attachment, P2 (figure 11). The distance between P1 and P2 is then used to calculate the magnetic contribution of the rail. The same method is used for both electrodes.

With this proposed method, the cathodic and anodic roots can move independently and with different velocities.

4.3. Results in a transient state

In this section, we present the circuit breaker results in a transient state using the approach of autonomous arc root displacement with possibilities of re-strike.

Figures 15(*a*)–(*d*) concern a transient case in air for a current intensity equal to 100 A. The temperatures are given at $t = 40$, 310, 580 and 870 μs, respectively. For $t = 310$ and 580 μs, we can observe a bending of the arc column towards the opposite side of the splitters. Indeed, the arc roots move more quickly than the arc centre due to the magnetic forces from the rails.

It is difficult to obtain experimental temperature and velocity measurements due to the arc motion and to the characteristics times of the phenomena. So in order to partially validate the model, figure 16 plots the mean velocity of the cathode and anode roots in an air plasma for a dc current of 100 A. This mean velocity is defined by

$$\bar{v} = \frac{[(\text{position at time } t) - (\text{position at time } t = 0)] \times 0.166}{\text{time}} \tag{17}$$

The value 0.166 is the grid spacing (in millimetres in the Ox-direction), which is constant in our case.

Experimental measurements exist in the literature giving the evolution of a low-voltage electric arc using a matrix of microcoils that behaves like a magnetic camera [16, 17]. The

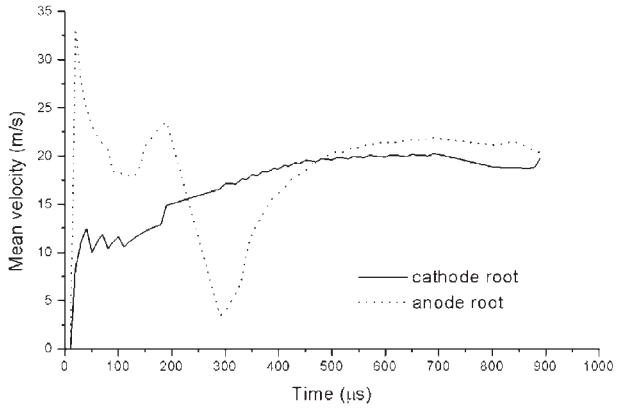

Figure 16. Arc root motion velocity versus time in an air plasma.

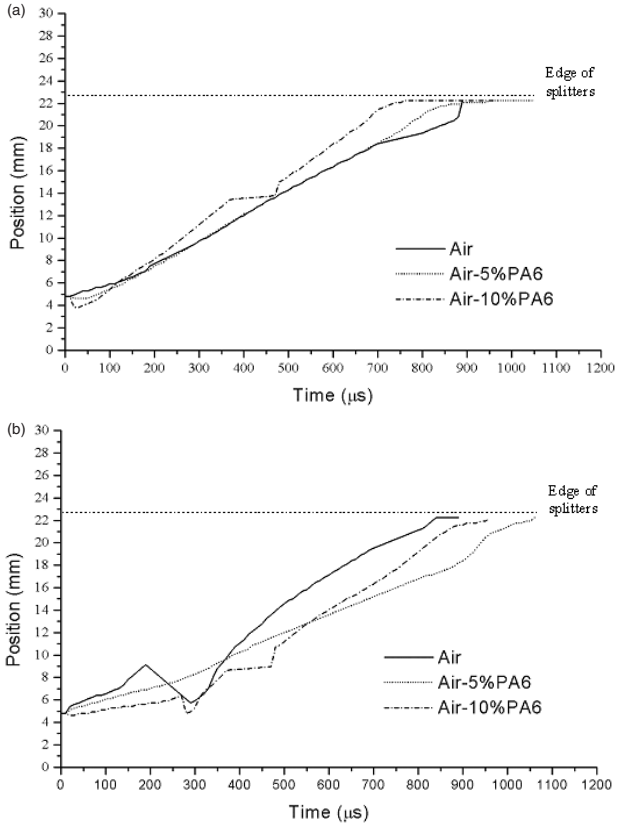

Figure 17. (*a*) Cathodic root position versus time and plasma composition. (*b*) Anodic root position versus time and plasma composition.

studies allow us to determine the average speed of the arc versus the peak value of the current and to determine the re-striking time. For a current of around 100 A, the mean velocity is around 10 m s^{-1} [16]. The re-striking velocity is estimated by the same authors at around 10 km s^{-1}.

We can note from figure 16 that the anode movement is more chaotic and that the mean velocity is around 10–20 m s^{-1}. The decrease between 200 and 300 μs corresponds to a back movement of the attachment. A slow decrease corresponds to a stagnation or back slide. We can also estimate from the model the theoretical re-striking time. The distance between 200 and 300 μs corresponds to 3 mm; we can then deduce the re-striking velocity as around 30 km s^{-1} in our case for a pure air plasma.

Although the model does not take into account all the physical mechanisms, it allows us to find the same order of magnitude of the time parameters and allows us to give an idea of the arc behaviour in the circuit breaker chamber. We are now going to use this model for a parametric study on the influence of the nature of the medium.

Figures 17(*a*) and (*b*) present the position of the cathodic and anodic roots versus time for the mixtures air, air–5%PA6 and air–10%PA6. The arc in air–5%PA6 slides from its initial position to the final one without re-strike. On the contrary, in the air and air–10%PA6 plasmas, a re-strike occurred on the anodic root position between 200 and 300 μs.

Of course, the homogeneous cases are far from the real situations, and the envisaged proportion of PA6 may be small for a current of a few kiloamperes. But this study shows the influence of the proportion of PA6 on arc behaviour and on the re-strike phenomenon.

Finally, for one case (air–5%PA6), we plot in figure 18, the axial current density distribution for three different planes, $k = 5, 17, 30$, corresponding to axial distances from the upper electrode equal to $z = 3.25$, 11 and 19.5 mm and for a given time $t = 700\,\mu$s. The figures represent the above views of the geometry. The rectangular grey surfaces correspond to the splitter and to the electrode. Due to the arc bending, the central position of the current density distribution varies along the z-direction. At the first and last positions, the current density distributions are less expanded due to the arc root attachment.

5. Conclusions

The aim of this work was to study the dynamics of the arc in the chamber of a low-voltage circuit breaker. Due to the numerous physical phenomena involved and to the complexity of the real device, the assumptions are used in a simplified geometry. Nevertheless, two specific points are studied: the influence of the proportion of PA6 and the external magnetic field on the arc movement.

First, the transport properties of air and mixtures of air and PA6 are calculated and discussed. The calculations show that the electrical conductivity decreases at low temperatures with the presence of PA6. At the same time, the thermal conductivity increases. These transport properties are tested in a three-dimensional stationary model of an arc at 100 A in a simplified circuit breaker geometry. The model estimates the effect of PA6 on the arc properties: the electrical potential increases with PA6 and organic vapours tend to decease the radial extension of the arc.

Still, with this stationary model, the influence of a constant external magnetic field on arc behaviour, according to the plasma composition, is studied. Two different values of the magnetic field are applied to shift the arc towards the splitters. It is shown that the total voltage drop increases with the value of the magnetic field and the presence of PA6.

Then, a transient state model is presented to study the displacement of the arc through the circuit breaker chamber. Two methods are proposed to deal with the magnetic field

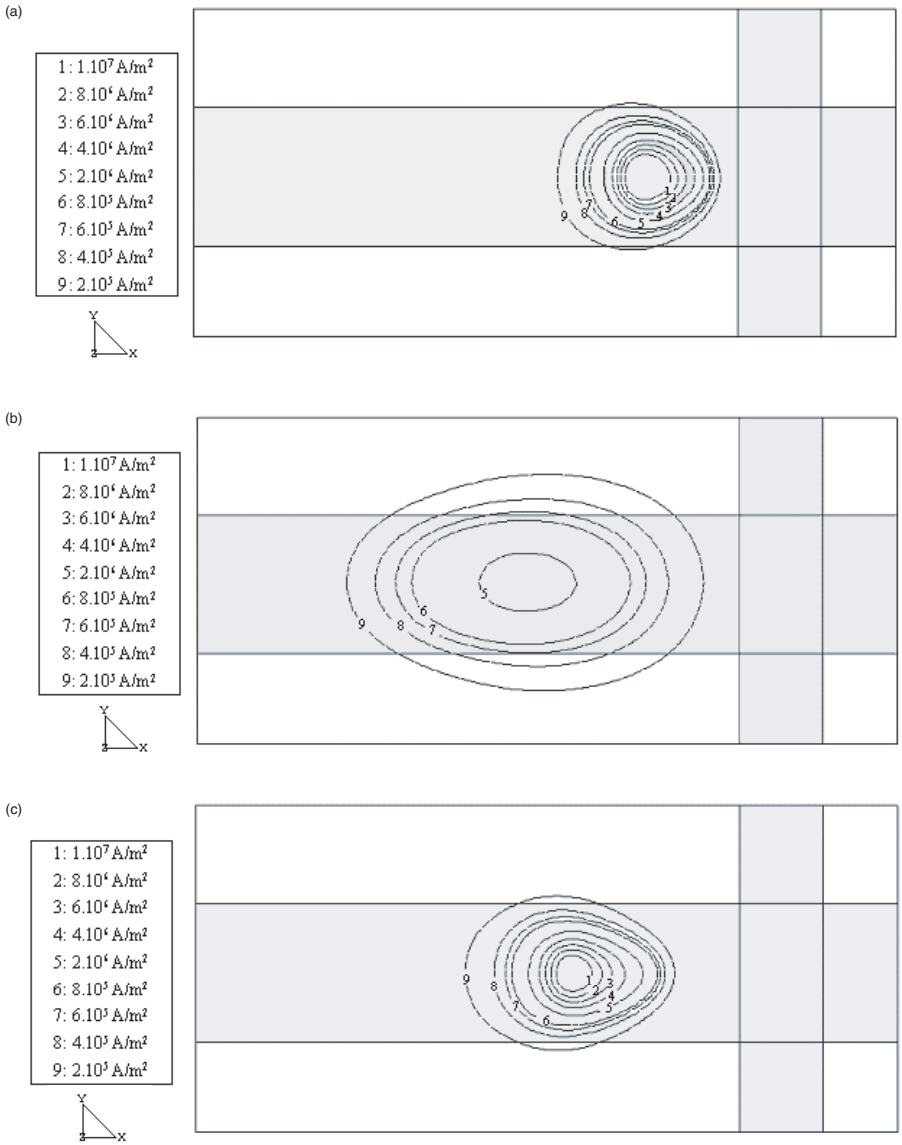

Figure 18. Current density distribution on the plane (*a*) $z = 3.25$ mm, (*b*) $z = 11$ mm and (*c*) $z = 19.5$ mm from the cathode (time: 700 μs) in air–5%PA6 medium; $I = 100$ A.

induced by the current contacts in the chamber and to describe a self-coherent displacement of the arc. This last point is based on the estimation of the local electrical conductivity and enables re-strikes of the arc.

Results of the transient model are then presented in the same simplified geometry at 100 A. The self-coherent displacement method is applied and the results for arc on the arc behaviour in the chamber are presented. It is shown that under forces, the arc roots are pushed towards the splitters as in the middle of the geometry, the arc seems to move more slowly. Finally, the behaviour of the arc in the presence of PA6 is studied in the transient case of the self-coherent movement.

Acknowledgments

We gratefully acknowledge EDF and Schneider Electric for their financial support.

6. References

[1] Kelkar M and Heberlein J 2000 *J. Phys. D: Appl. Phys.* **33** 2172–82
[2] Schlitz L Z, Garimella S V and Chan S H 1999 *J. Appl. Phys.* **85** 2547–55
[3] Blais A, Proulx P and Boulos M I 2003 *J. Phys. D: Appl. Phys.* **36** 488–96
[4] Fang M T C and Banks A D J 1985 *J. Phys. D: Appl. Phys.* **18** 229–38
[5] Karetta F and Lindmayer M 1998 *IEEE Trans. Components* **21** (part A) 96–103
[6] Swierczynski B, Gonzalez J J, Freton P and Gleizes A 2003 Contribution 3D à l'étude d'un disjoncteur Basse Tension 6èmes journées d'études sur les fluctuations des arcs (Clermont-Ferrand, France) II-12
[7] Stammberger H, Daube T, Dehning C and Anheuser M 2002 Arc simulations in realistic low-voltage arcing chambers *Int. Conf. on Electrical Contacts (Zurich)* ed W Johler (Switzerland: Swiss Electrotechnical Association)

[8] Brdys C, Toumazet J P, Laurent A and Ponthenier J L 2002 *Meas. Sci. Technol.* **13** 1146–53
[9] Fievet C, Barrault M, Petit P, Chevrier P, Fleurier C and Andre V 1997 *J. Phys. D: Appl. Phys.* **30** 2991–9
[10] Lindmayer M 2002 *Proc. 14th Int. Conf. on Gas Discharges and their Applications (Liverpool)* vol 2, pp 318–24
[11] Daube T, Stammberger H, Anheuser M and Dehning C 2001 3D simulation of a low-voltage switching arc based on MHD equations *14th Symp. on Physics of Switching Arc, FSO Czech Republic (Brno)* pp 45–50
[12] Schlitz L Z, Garimella S V and Chan S H 1999 *J. Appl. Phys.* **85** 2540–6
[13] Lindmayer M 2002 Simulation of switching devices based on the general transport equation *Int. Conf. on Electrical Contacts (Zurich)* ed W Johler (Switzerland: Swiss Electrotechnical Association)
[14] Barcikowski F and Lindmayer M 2000 Simulations of the heat balance in low-voltage switchgear *Int. Conf. on Electrical Contacts (Stockholm)*
[15] Essiptchouk A M, Sharakhovsky L I and Marotta A 2000 *J. Phys. D: Appl. Phys.* **33** 2591–7
[16] Mercier M, Cajal D, Laurent A, Velleaud G and Gary F 1996 *J. Phys. D: Appl. Phys.* **29** 95–8
[17] Cajal D, Laurent A, Gary F, Mercier M and Servant S 1999 *J. Phys. D: Appl. Phys.* **32** 1130–5
[18] Doméjean E, Chévrier P, Fiévet C and Petit P 1997 *J. Phys. D: Appl. Phys.* **30** 2132–42
[19] Bu W H, Fang M T C and Guo Z Y 1990 *J. Phys. D: Appl. Phys.* **23** 175–83
[20] Chevrier P, Barrault M, Fievet C, Matfoul J and Millon Frémillon J 1997 *J. Phys. D: Appl. Phys.* **30** 1346–55
[21] Andre P 1997 *J. Phys. D: Appl. Phys.* **30** 475
[22] Andre P 1996 *J. Phys. D: Appl. Phys.* **29** 1963
[23] Godin D 1998 Mémoire de maîtrise es sciences, University of Montreal (in French)
[24] Godin D and Trépanier J Y 1999 *Proc. 14th International Symp. on Plasma Chemistry (Praha, Czech Republic)* vol 1, p 239
[25] Chervy B, Gleizes A and Razafinimanana M 1994 *J. Phys. D: Appl. Phys.* **27** 1193
[26] Hirschfelder J O, Curtis C F and Byron B R 1964 *Molecular Theory of Gases and Liquids* (New York: Wiley)
[27] Devoto R S 1967 *Phys. Fluids* **10** 2105
[28] Devoto R S 1966 *Phys. Fluids* **9** 1230
[29] Vanderslice J T, Weissman S, Mason E A and Fallon R J 1962 *Phys. Fluids* **5** 155
[30] Muckenfuss C and Curtiss C F 1958 *J. Chem. Phys.* **29** 1273
[31] Devoto R S 1967 *Phys. Fluids* **10** 354
[32] Butler J N and Brokaw R S 1957 *J. Chem. Phys.* **26** 1636
[33] Neufeld Ph D, Janzen A R and Aziz R A 1972 *J. Chem. Phys.* **57** 1100
[34] Tan C W 1963 *PhD Thesis* University of Illinois, No 64-6163
[35] Kihara T, Taylor M H and Hirschfelder J O 1960 *Phys. Fluids* **3** 715
[36] Mason E A, Munn R J and Smith F J 1967 *Phys. Fluids* **10** 1827
[37] Capitelli M, Gorse C, Longo S and Giordano D 1998 AIAA paper no 98-2936 *7th AIAA/ASME Joint Thermophysics and Heat Transfer Conf. (Albuquerque, NM)*
[38] Belov V A and Semenov A M 1971 *High Temp.* **9** 253
[39] Belov V A and Semenov A M 1971 *High Temp.* **9** 654
[40] Aubreton J 1985 *PhD Thesis* University of Limoges, France
[41] Aubreton J and Fauchais P 1983 *Rev. Phys. Appl.* **18** 51
[42] Sanon A 1988 *PhD Thesis* University of Limoges, France
[43] Freton P, Gonzalez J J and Gleizes A 2000 *J. Phys. D: Appl. Phys.* **33** 2442–52
[44] Gonzalez J J, Freton P and Gleizes A 2002 *J. Phys. D: Appl. Phys.* **35** 3181–91
[45] Freton P, Gonzalez J J, Gleizes A, Camy Peyret F, Caillibotte G and Delzenne M 2002 *J. Phys. D: Appl. Phys.* **35** 115–31
[46] Patankar S V 1980 *Heat Transfer and Fluid Flow* (NewYork: McGraw-Hill)
[47] Kweon K Y, Yan J D and Fang M T C 2003 *Proc. 15th Symp. on Phys. Switching Arc* (Brno, Czech Republic, 22–26 September) vol 1
[48] Girard R 2000 *Thesis* Université Paul Sabatier, France, No 3713
[49] Baudy C, Mariaux G, Vardelle A, Delalondre C and Meillot E 2003 *Proc. 16th Int. Symp. on Plasma Chem. ISPC 16 (Taormina, Italy, 22–27 June)*
[50] Bauchire J M, Gonzalez J J and Gleizes A 1997 *Plasma Chem. Plasma Process.* **17** 409